Time-Scales of Charge Relaxation in a Superconducting Island via an Inductive Shunt

bachelor's thesis

Submitted to the Faculty of Mathematics, Computer Science and Natural Sciences

presented by

Lisa Arndt

under the supervision of

Prof. Dr. Fabian Hassler

Institute for Quantum Information

07/2015

Contents

Ich versichere hiermit, dass ich die Arbeit selbstständig verfasst und keine anderen als die angegebenen Quellen und Hilfsmittel benutzt sowie Zitate kenntlich gemacht habe.

Aachen, den 07.07.2015

Lisa Arndt

Chapter 1

Introduction

1.1 Introduction and chapter overview

This thesis deals with the topic of charge relaxation in superconducting islands. First discovered in 1911 [11], superconductivity still constitutes an interesting field of modern condensed matter physics. The phenomena is the result of small net effective attractions between the electrons due to interactions between them and the vibrations of the atoms in the lattice [4]. Because of these attractions, two electrons can form a so-called Copper pair but, since the pairing energy is very weak, the temperature must be sufficiently low for a Cooper pair to exist.

In this thesis, we will take a closer look at a superconducting island that is connected to a bulk superconductor via a Josephson junction. The Hamiltonian of this Cooper pair box is 2π-periodic in the superconducting phase difference. The problem can therefore be formulated in the basis of Bloch waves, where the Bloch momentum is equivalent to the continuous part of the charge on the island and remains conserved. If an inductive shunt is added to the Cooper pair box, the Bloch momentum turns into a dynamic variable. Next, we can therefore discuss the mechanism of charge relaxation on the superconducting island. The inductive shunt to the ground also gives the possibility of screening the effect of charge noise. A Cooper pair box can represent a quantum bit and charge noise can cause this qubit to dephase, losing its intrinsic quantum mechanical properties. It is therefore valuable for quantum information to know how to screen the Cooper pair box against charge noise.

Chapter 2 of this thesis focuses on the band structure of the Cooper pair box and the size of the band gaps which depend strongly on the Josephson energy. We also consider the influence of the inductive shunt which breaks the 2π-

periodicity of the former Hamiltonian and couples the bands. In Ch. 3, we will discuss the transition probability between bands when a semi-classical charge state travels through the band structure. Here, we discover that we can divide our problem into two regimes dependent on the initial charge and the setup parameters: In the first regime, where the Josephson energy responsible for the formation of bands can be neglected, we only have to consider the inductive shunt. Here, it will be useful to discard the Bloch wave base and rather concentrate on the fact that the remaining Hamiltonian has the form of an harmonic oscillator. In the second regime, no transition between bands occurs and we can therefore neglect the transition probability between bands. Here, our problem reduces to that of a single band structure.

After establishing both regimes, we will start to consider charge relaxation and the possibility of screening the circuit from charge noise in both regimes. In Ch. 4, we begin by calculating the time scales of a wave packet in the charge base that was prepared at an initial charge. This is followed by a discussion of charge relaxation due to a time dependent perturbation resulting from charge noise in Ch. 5, where we will also discuss the implications of our result regarding the screening of our system against charge noise.

1.2 About superconductors

In contrast to an electron, which is a Fermi particle, a Cooper pair acts as a Bose particle. Therefore more than one Cooper pair can be in the same state. As a result of this, nearly all Cooper pairs will be locked down in the same state at the lowest energy [4]. Now, if Ψ is the wave function of one Cooper pair in an environment with a high number of pairs, then $P = \Psi\Psi^*$ can be interpreted as a particle density (or charge density ρ, if multiplied by q). Since this is the case in a superconductor, we can rewrite Ψ with the square root of the charge density ρ and a phase factor Θ (both real functions of $\boldsymbol{r}$) as [4]

$$\Psi(\boldsymbol{r}) = \rho(\boldsymbol{r})^{\frac{1}{2}} e^{i\Theta(\boldsymbol{r})}. \tag{1.1}$$

In this context, both ρ and Θ have a direct physical interpretation. While the physical interpretation of ρ is clear, we will take a closer look at the current density $\boldsymbol{J}$, which is defined via the continuity equation

$$\boldsymbol{\nabla} \cdot \boldsymbol{J} = -\frac{\partial P}{\partial t}, \tag{1.2}$$

to explore the physical interpretation of Θ. The current density has a direct physical interpretation as the current density in a superconductor. In order to express $\boldsymbol{J}$ in terms of ρ and Θ, we need to use the Schrödinger equation of a particle with charge q that is moving in an electromagnetic field with the electric potential ϕ and the vector potential $\boldsymbol{A}$ [4]

$$-\frac{\hbar}{i}\frac{\partial\Psi}{\partial t} = \hat{H}\Psi = \frac{1}{2m}\left(\frac{\hbar}{i}\boldsymbol{\nabla} - q\boldsymbol{A}\right)^2\Psi + q\phi\Psi. \tag{1.3}$$

If we use the Schrödinger equation and Eq. (1.1), we can rewrite the current density as

$$\boldsymbol{J} = \frac{\hbar}{m}\left(\boldsymbol{\nabla}\Theta - \frac{q}{\hbar}\boldsymbol{A}\right)\rho. \tag{1.4}$$

Now, the physical interpretation of Θ is obvious. While the absolute phase is not observable, the gradient of the phase can be measured through the current density. If we know the gradient of the phase everywhere, we know the phase everywhere, except for a constant.

With this information, we can take a closer look at the so-called Josephson junction which will be an important part of this thesis. The Josephson junction consists of two superconductors divided by a thin insulating barrier. If the insulating barrier is small enough, Cooper pairs can jump from on side of the barrier to the other.

The current I and the voltage U across the junction are both defined by the phase difference φ of the wave function on both sides of the barrier (the constant I_c is the critical current of the junction and depends on the specific setup) via [1]

$$I = I_c\sin(\varphi) \quad \text{and} \quad U = \frac{\hbar}{2e}\frac{\partial\varphi}{\partial t}. \tag{1.5}$$

This is an example where the phase difference can be directly observed through the measurement of the current or the voltage. Now, we can begin to consider the Hamiltonian of an inductively shunted Cooper pair box in the next chapter.

Chapter 2

The inductively shunted CPB

2.1 The Hamiltonian of the inductively shunted CPB

The Hamiltonian of an inductively shunted Josephson junction, as seen in Fig. 2.1, can be written as [6]

$$\hat{H} = \underbrace{4E_C(\hat{n} - n_g)^2 - E_J \cos(\hat{\varphi})}_{\hat{H}_{\mathrm{CPB}}} + \frac{1}{2} E_L \hat{\varphi}^2 \tag{2.1}$$

assuming that there is no external magnetic flux. Here, the first two terms constitute the Hamiltonian $\hat{H}_{\mathrm{CPB}}$ of a Cooper pair box — a superconducting island connected to the ground superconductor via a Josephson junction — while the third term is due to the inductive shunt.

The operator $\hat{n} = \hat{q}/2e$ measures the charge on the island in units of the charge of a Cooper pair and $\hat{\varphi}$ measures the phase difference across the junction, see Sec. 1.2. Both operators obey the relation $[\hat{\varphi},\hat{n}]=i$. Our problem depends on

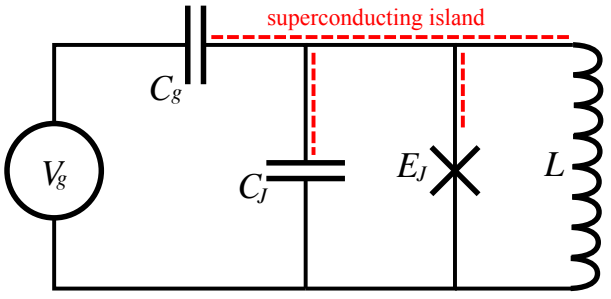

Figure 2.1: Circuit of an inductively shunted Josephson junction E_J with inductance L, voltage source V_g, and the two capacities C_g and C_J. Without the inductance a superconducting island forms on the upper part of the circuit.

three different energy scales:

i) the charging energy $E_C = e^2/2(C_J + C_g)$ [6] resulting from the capacity C_J, connected in parallel with the Josephson junction, and the capacity C_g, connected in series with the voltage source V_g,

ii) the Josephson energy $E_J = \Phi_0 I_c/2\pi$ with the critical current I_c and the flux quantum $\Phi_0 = h/2e$, and

iii) the inductive energy $E_L = (\Phi_0/2\pi)^2/L$ [6] resulting from the inductive shunt L.

The effect of the voltage source V_g is incorporated through the offset charge n_g via $n_g = C_g V_g/2e$.

Since this thesis focuses on the effects of the inductive shunt with large inductance L, our calculations will be set in the semi-classical regime $E_L \ll 8E_C$. For the following chapters, it will also be useful to apply the gauge transformation

$$\Psi \mapsto e^{i\hat{\varphi}\, n_g}\Psi \tag{2.2}$$

which transforms the effective Hamiltonian to

$$\hat{H} = 4E_C\hat{n}^2 - E_J\cos(\hat{\varphi}) + \frac{1}{2}E_L\hat{\varphi}^2 + \dot{n}_g(t)\hat{\varphi}. \tag{2.3}$$

This form highlights that the spectrum does not depend on static n_g which will be the case we assume for the following calculations, unless denoted otherwise.

2.2 The CPB without an inductive shunt

In this section, we will start by considering only the CPB part of the Hamiltonian. Since $\hat{H}_{\mathrm{CPB}}$ has a periodic potential in the phase basis $\{|\varphi\rangle\}$, it is useful to transform the Hamiltonian into the basis of Bloch waves $\{|s,p\rangle\}$ with the corresponding normalized wave functions $\langle\varphi|s,p\rangle = \psi_{s,p}(\varphi) = e^{ip\varphi}u_{s,p}(\varphi)/\sqrt{2\pi}$. Here, $s \in \mathbb{N}$ denotes the band index and $p \in (-1/2, 1/2]$ the quasi momentum. The function $u_{s,p}(\varphi)$ is periodic in 2π since $\hat{H}_{\mathrm{CPB}}$ has the same periodicity.

The Hamiltonian $\hat{H}_{\mathrm{CPB}}$ is diagonal in the basis of Bloch waves due to its peri-

odicity in φ and we can write

$$\begin{aligned}\langle\varphi|\,\hat{H}_{CPB}\,|s,p\rangle &= \frac{1}{\sqrt{2\pi}}\left[4E_C\left(-i\frac{\partial}{\partial\varphi}\right)^2 - E_J\cos(\varphi)\right]e^{ip\varphi}u_{s,p}(\varphi)\\ &= \frac{1}{\sqrt{2\pi}}e^{ip\varphi}\left[4E_C\left(-i\frac{\partial}{\partial\varphi}+p\right)^2 - E_J\cos(\varphi)\right]u_{s,p}(\varphi)\\ &= \frac{1}{\sqrt{2\pi}}e^{ip\varphi}\,\varepsilon_s(p)\,u_{s,p}(\varphi).\end{aligned} \tag{2.4}$$

To determine the eigenvalues $\varepsilon_s(p)$ of the Hamiltonian $\hat{H}_s(p)$, we use the standard representation of the charge states $\langle\varphi|n\rangle = e^{in\varphi}/\sqrt{2\pi}$ to calculate the matrix elements

$$\begin{aligned}\left\langle n'\right|\cos(\hat{\varphi})\,|n\rangle &= \frac{1}{4\pi}\int_{-\infty}^{\infty}\left[e^{i\varphi(n-n'+1)} + e^{i\varphi(n-n'-1)}\right]d\varphi\\ &= \frac{1}{2}\left(\delta_{n',n+1} + \delta_{n',n-1}\right).\end{aligned} \tag{2.5}$$

In the charge basis $\{|n\rangle\}$, the Hamiltonian $\hat{H}_s(p)$ can therefore be written as a sparse matrix with the diagonal elements $\langle n|\,\hat{H}_s(p)\,|n\rangle = 4E_C(n+p)^2$ and the off-diagonal elements $-E_J/2$

$$\begin{pmatrix}
\ddots & \ddots & & & & & \\
\ddots & 4E_C(-2+p)^2 & -\frac{E_J}{2} & & & \underline{0} & \\
 & -\frac{E_J}{2} & 4E_C(-1+p)^2 & -\frac{E_J}{2} & & & \\
 & & -\frac{E_J}{2} & 4E_Cp^2 & -\frac{E_J}{2} & & \\
 & & & -\frac{E_J}{2} & 4E_C(1+p)^2 & -\frac{E_J}{2} & \\
 & \underline{0} & & & -\frac{E_J}{2} & 4E_C(2+p)^2 & \ddots \\
 & & & & & \ddots & \ddots
\end{pmatrix} \tag{2.6}$$

While we can not determine the eigenvalues and -vectors of this matrix analytically, they can be easily calculated numerically because of the sparse form of our matrix. To calculate the eigenvalues $\varepsilon_s(p)$ for $s = 1, ..., 5$, we use a reasonable amount of charge states $n = -10, ..., 10$ to get a good accuracy for our number of bands and express our result dependent on the dimensionless quantity $\eta = E_J/4E_C$. The resulting eigenvalues $\varepsilon_s(p)$ for $\eta = 0.1$ and $\eta = 0.7$ are displayed in Fig. 2.2. Here, the band structure and the η-dependent energy

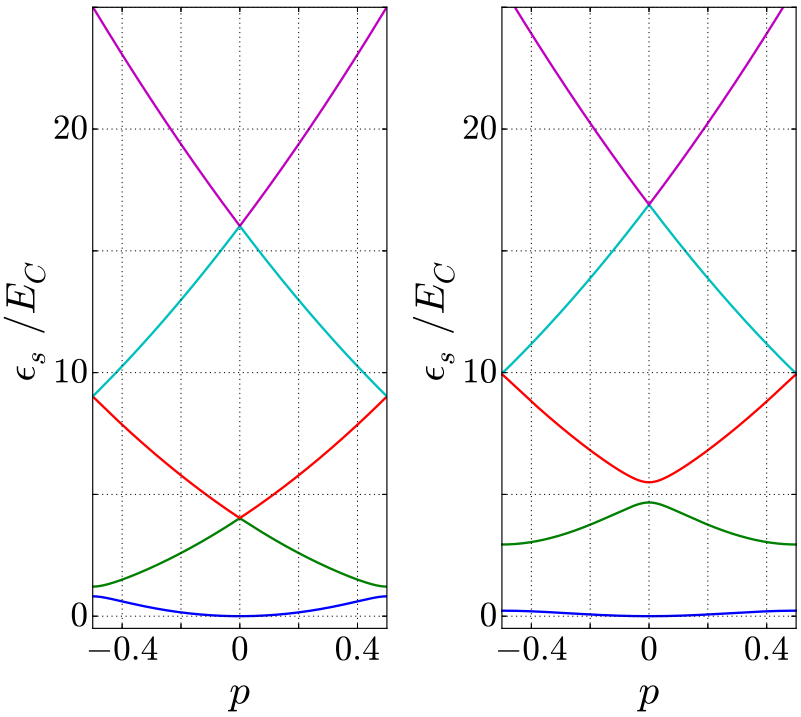

Figure 2.2: Numerical calculation of the band structure of the CPB with the Hamiltonian $\hat{H}_s(p)$ in the Bloch wave base for $\eta = E_J/4E_C = 0.1$ (left) and $\eta = 0.7$ (right). The size of the band gap is strongly dependent on η and the band index s. In the left figure, the band gaps are barely visible while in the right figure the band gaps become more prominent, especially in the lower bands. In general, the band gaps become larger in lower bands.

splitting is clearly visible: For $\eta = 0.1$, the bands correspond very well to the "nearly free electron approximation" of solid state physics where bands can be described via the band structure of free electrons with a lifting of degeneracy at the Brillouin zone boundary. For $\eta = 0.7$, this approximation no longer holds as the band gap between the first two bands becomes very large while the gap between $s = 2$ and $s = 3$ begins to show.

2.3 The inductive shunt

After considering only the CPB part of the Hamiltonian in the last section, we will now try to include the inductive term in our calculations as well. While the Cooper pair box has a periodic potential in the phase basis, this is no longer the case when we include the inductive shunt in our calculations. An intuitive way of understanding this is that the island in the CPB is eliminated by the inductive shunt and therefore our charge is now rendered continuous. However,

in our limit of large inductance $E_L \ll 8E_C$, the periodicity is only weekly broken and it is therefore still useful to take a closer look at our Hamiltonian in the Bloch wave base.

In the Bloch wave base, we can write $\hat{\varphi} = id/dp + \Omega$ with the Hermitian operator Ω that causes inter-band coupling and can be defined via [6]

$$\langle s,p|\,\Omega\,|s',p'\rangle = \delta(p-p')\frac{i}{2\pi}\int_0^{2\pi} u^*_{s,p}(\varphi)\frac{du_{s',p}(\varphi)}{dp}d\varphi. \tag{2.7}$$

This result can be obtained by rewriting $\langle s,p|\,\hat{\varphi}\,|s',p'\rangle$ as

$$\begin{aligned}\langle s,p|\,\hat{\varphi}\,|s',p'\rangle &= \frac{1}{2\pi}\int_{\mathbb{R}} e^{i\varphi(p'-p)}\,\varphi\,u^*_{s,p}(\varphi)\,u_{s',p'}(\varphi)d\varphi \\ &= \frac{1}{2\pi}\int_{\mathbb{R}} i\frac{d}{dp}\left(e^{i\varphi(p'-p)}\,u^*_{s,p}(\varphi)\,u_{s',p'}(\varphi)\right)d\varphi \\ &\qquad - \frac{1}{2\pi}\int_{\mathbb{R}} ie^{i\varphi(p'-p)}u_{s',p'}(\varphi)\frac{du^*_{s,p}(\varphi)}{dp}d\varphi.\end{aligned} \tag{2.8}$$

Now, the first term can be written as $id/dp\,\delta_{ss'}\delta(p-p')$, if we use the orthogonal properties of the Bloch wave functions. This is the first part of our operator $\hat{\varphi}$. To simplify the second term, we make use of the fact that $u_{s,p}(\varphi)$ is periodic in 2π and that p is restricted to $(-1/2, 1/2]$. We then apply the Poisson summation formula to obtain

$$\begin{aligned}&-\frac{1}{2\pi}\int_{\mathbb{R}} ie^{i\varphi(p'-p)}\underbrace{u_{s',p'}(\varphi)\frac{du^*_{s,p}(\varphi)}{dp}}_{2\pi\text{-periodic}}d\varphi \\ &= -\frac{1}{2\pi}\sum_{m\in\mathbb{Z}} e^{i2\pi m(p'-p)}\int_0^{2\pi} ie^{i\varphi'(p'-p)}u_{s',p'}(\varphi')\frac{du^*_{s,p}(\varphi')}{dp}d\varphi' \\ &= -\delta(p-p')\frac{i}{2\pi}\int_0^{2\pi} u_{s',p}(\varphi')\frac{du^*_{s,p}(\varphi')}{dp}d\varphi' \\ &= -\delta(p-p')\frac{i}{2\pi}\int_0^{2\pi}\left\{\frac{d}{dp}\left[u_{s',p}(\varphi')u^*_{s,p}(\varphi')\right] - u^*_{s,p}(\varphi)\frac{du_{s',p}(\varphi)}{dp}\right\}d\varphi' \\ &= \delta(p-p')\frac{i}{2\pi}\int_0^{2\pi} u^*_{s,p}(\varphi)\frac{du_{s',p}(\varphi)}{dp}d\varphi' = \delta(p-p')\,\Omega_{s,s'}(p).\end{aligned} \tag{2.9}$$

Here, we have exploited orthogonality of the Bloch wave functions $u_{s,p}(\varphi)$ to obtain the last line which is just Eq. (2.7).

While Ω is diagonal in p, it is not diagonal in s since Ω is responsible for coupling different bands with each other. To get a better understanding for

Ω, we will rewrite $\Omega_{s,s'}(p)$ for $s \neq s'$ using the Hamiltonian $\hat{H}_s(p)$. First, we differentiate both sides of the time-independent Schrödinger equation of $\hat{H}_s(p)$, see Eq. (2.4), with respect to p

$$\hat{H}'_s(p)\left|u_{s',p}\right\rangle + \hat{H}_s(p)\frac{d}{dp}\left|u_{s',p}\right\rangle = \varepsilon'_{s'}(p)\left|u_{s',p}\right\rangle + \varepsilon_{s'}(p)\frac{d}{dp}\left|u_{s',p}\right\rangle. \tag{2.10}$$

Now, we can multiply both sides by $\langle u_{s,p}|$

$$\langle u_{s,p}|\,\hat{H}'_s(p)\left|u_{s',p}\right\rangle + \varepsilon_s(p)\,\langle u_{s,p}|\,\frac{d}{dp}\left|u_{s',p}\right\rangle = \varepsilon_{s'}(p)\,\langle u_{s,p}|\,\frac{d}{dp}\left|u_{s',p}\right\rangle. \tag{2.11}$$

and solve the equation for $\langle u_{s,p}|\, id/dp\left|u_{s',p}\right\rangle$ which is identical to $\Omega_{s,s'}(p)$

$$\langle u_{s,p}|\, i\frac{d}{dp}\left|u_{s',p}\right\rangle = i\frac{\langle u_{s,p}|\,\hat{H}'_s(p)\left|u_{s',p}\right\rangle}{\varepsilon_{s'}(p)-\varepsilon_s(p)}. \tag{2.12}$$

Since our matrix element $\Omega_{s,s'}(p)$ is inversely proportional to the band gap between s and s', the directly adjacent bands form the largest contribution to the matrix. In addition, the value of one matrix element will strongly depend on p since the band gap varies highly with p for $\eta \lesssim 1$ and is smallest for $p = 0$ or $p = 1/2$, see Fig. 2.2. If we use the numerically calculated eigenvectors from the matrix in Eq. (2.6) and rewrite $\langle u_{s,p}|\,\hat{H}'_s(p)\left|u_{s',p}\right\rangle$ as

$$\begin{aligned}\langle u_{s,p}|\,\hat{H}'_s(p)\left|u_{s',p}\right\rangle &= \sum_{n\in\mathbb{Z}}\langle u_{s,p}|\,8E_C(\hat{n}+p)\,|n\rangle\,\langle n|u_{s',p}\rangle \\ &= \sum_{n\in\mathbb{Z}} 8E_C(n+p)\,\langle n|u_{s,p}\rangle^*\,\langle n|u_{s',p}\rangle\,,\end{aligned} \tag{2.13}$$

we are able to calculate $\Omega_{s,s'}(p)$ numerically. The results can be found in Fig. 2.3. If we compare both figures, we can clearly make out that the peaks at $p = 1/2$ and $p = 0$ are the larger the smaller η and therefore they are the larger the smaller the band gap at those critical points. The same argument applies to higher band indexes since the band gaps become smaller with higher bands, see Fig. 2.2.

To analyze Ω even further, we will now take an exemplary look at the matrix element between band one and two at $p = 1/2$ since this is the point where the band gap closes and a crossing forms for $E_J = 0$. In order to get an analytic expression for Ω, we will assume the case of $E_J \ll 4E_C$ and use perturbation theory to calculate the eigenvalues and -vectors of our problem at $p = 1/2$.

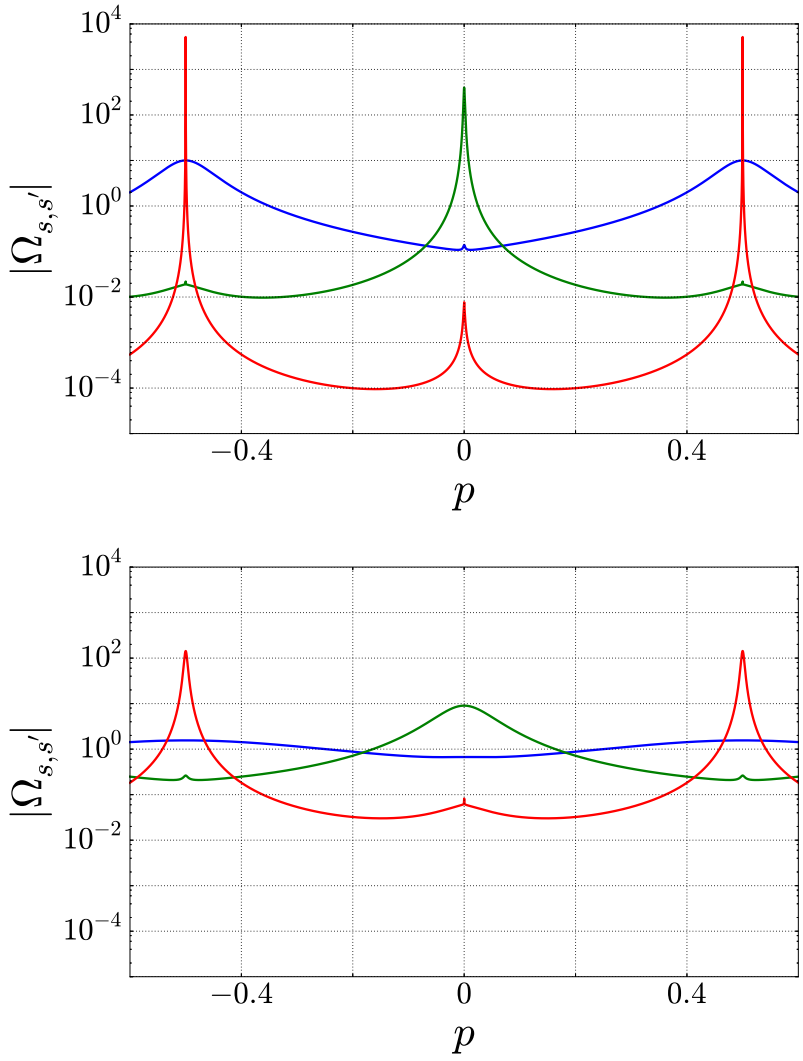

Figure 2.3: Size of Ω, which causes band coupling, for three different band gaps $\Omega_{1,2}$ (blue), $\Omega_{2,3}$ (green), and $\Omega_{3,4}$ (red). $\Omega_{s,s'}$ is periodic in p with periodicity 1. The top figure shows the band gaps for $\eta = E_J/4E_C = 0.1$ and the bottom figure shows the band gaps for $\eta = 0.7$. It is clearly visible that $\Omega_{s,s'}$ is inversely proportional to the size of the band gap, see Fig. 2.2. Therefore the peaks become larger with smaller η and higher bands s and s'.

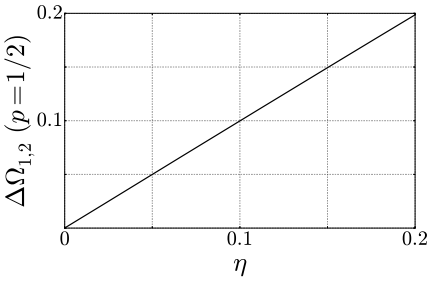

Figure 2.4: Numerical evaluation of the scaling of $\Delta\Omega_{1,2}(p = 1/2)$, which is the width of the peak of $\Omega_{s,s'}$ at $p = 1/2$ between band $s = 1$ and $s = 2$, for small $\eta = E_J/4E_C$. The linear dependency of $\Delta\Omega_{1,2}(p = 1/2)$ on η is clearly visible.

We will therefore divide the Hamiltonian $\hat{H}_s(p)$ into $\hat{H}_0 = 4E_C(\hat{n} + 1/2)^2$ with the eigenvectors $|n\rangle$ and the small perturbation $\hat{V} = -E_J \cos(\hat{\varphi})$. Since $\hat{H}_0$ is degenerate in $n = 0$ and $n = -1$, we need to use degenerate perturbation theory for our calculations. Using Eq. (2.5), we can write the perturbation $\hat{V}$ of the two-level system as

$$\hat{V} = \begin{pmatrix} 0 & -\frac{1}{2}E_J \\ -\frac{1}{2}E_J & 0 \end{pmatrix}. \tag{2.14}$$

This matrix has the eigenvalues $\pm E_J/2$ with the correspondent eigenvectors

$$\boldsymbol{v}_+ = \frac{1}{\sqrt{2}} \begin{pmatrix} 1 \\ -1 \end{pmatrix} \qquad \text{and} \qquad \boldsymbol{v}_- = \frac{1}{\sqrt{2}} \begin{pmatrix} 1 \\ 1 \end{pmatrix}. \tag{2.15}$$

To leading order, we therefore obtain two eigenvalues $E_0^1 = E_C + E_J/2$ and $E_0^2 = E_C - E_J/2$ with the associated eigenvectors $\left|E_0^1\right\rangle = (|0\rangle - |-1\rangle)/\sqrt{2}$ and $\left|E_0^2\right\rangle = (|0\rangle + |-1\rangle)/\sqrt{2}$ in the charge base. We can already see that the band gap scales with E_J and with this information we can use Eq. (2.12) to find that $\Omega_{1,2}(p = 1/2) = 1/\eta$.

Besides the scaling of the peak of $\Omega_{1,2}$ at $p = 1/2$, another interesting information is the scaling of the width of the peak. We can gather this information numerically by using the same algorithm as before, see Eq. (2.13) and (2.12), and defining the width as the difference between the two points at which $\Omega_{1,2}$ has decreased to halve its size. This calculation yields the result $\Delta\Omega_{1,2}(p = 1/2) = \eta$ for small η and can be found in Fig. 2.4. Consequently, our calculations suggest that Ω will assume the form of a δ-distribution for $\eta \to 0$. The interpretation of this result will be discussed in the next chapter.

Chapter 3

Transition probability between bands

3.1 Band gap via Brillouin-Wigner perturbation theory

In the last chapter, we tried to evaluate Ω, which is the part of our Hamiltonian causing inter-band coupling and therefore transitions between bands, using numerical and analytic methods. However, since we are ultimately interested in the transition probability between bands, this chapter will focus on approximating this probability directly using the Landau-Zener formula.

In order to use this formula, we first need to find a way to calculate the band gap between two adjacent bands or in other words, the off-diagonal element Δ of the two-level system's Hamiltonian coupling the bases which can be written as [1]

$$\hat{H}_{n,n'} = \begin{pmatrix} E_n & \Delta \\ \Delta & E_{n'} \end{pmatrix}. \tag{3.1}$$

While we have already calculated the band gap numerically (and analytically for one exemplary gap, see Sec. 2.3), we now want to find a general analytic expression for $E_J \ll 4E_C$. We will therefore divide our Hamiltonian $\hat{H}_s(p)$ in the same two parts as in the end of the last section and again express our problem through the unperturbed charge states $|n\rangle$ for $E_J = 0$ with the energy $\varepsilon_{0,n} = 4E_C(n+p)^2$ and the small perturbation $\hat{V} = -E_J\cos(\hat{\varphi})$. Now, the Brillouin-Wigner perturbation theory allows us to calculate the matrix element

[1] Note that Δ is in fact only halve the size of the band gap, because it can be written as the off-diagonal element of our two-level system's Hamiltonian.

Δ to leading order in $\eta = E_J/4E_C$ by using the formula (see App. A)

$$\Delta_{n,n'} = \frac{\langle n|\,\hat{V}\,|n-1\rangle\,\langle n-1|\,\hat{V}\,|n-2\rangle\cdots\langle n'+1|\,\hat{V}\,|n'\rangle}{(\varepsilon_{0,n}-\varepsilon_{0,n-1})(\varepsilon_{0,n}-\varepsilon_{0,n-2})\cdots(\varepsilon_{0,n}-\varepsilon_{0,n'+1})}. \tag{3.2}$$

We are interested in the points $p = 0$ and $p = 1/2$. For $p = 0$, states $|n\rangle$ and $|-n\rangle$ of the Hamiltonian $\hat{H}_0$ are degenerate and span the two-level system that we will study in this particular case. For $p = 1/2$, our two-level system will be constituted by the states $|n\rangle$ and $|-n-1\rangle$.

We start with the numerator of $\Delta_{n,n'}$ which simplifies to $(-E_J/2)^{2n}$ (for $p = 0$) or $(-E_J/2)^{2n+1}$ (for $p = 1/2$), if we use Eq. (2.5). For the denominator of $\Delta_{n,n'}$, we can write

$$\begin{aligned}
&(4E_C)^{2n-1}\prod_{k=1}^{2n-1}k(2n-k) = (4E_C)^{2n-1}\left[(2n-1)!\right]^2, \text{ for } p=0 \text{ or}\\
&(4E_C)^{2n}\prod_{k=1}^{2n}k(2n+1-k) = (4E_C)^{2n}\left(2n!\right)^2, \qquad \text{for } p=\frac{1}{2}.
\end{aligned} \tag{3.3}$$

We will now introduce the notation $q = n + p$ which we will use repeatedly in the next chapters. The new variable q corresponds to the complete charge on the superconducting island with the continuous part of the charge in form of the Bloch momentum p and the discrete charge n. For our current calculations, q will be a half-integer as we are only calculating the band gap at the interesting points $p = 1/2$ and $p = 0$. Using this new notation and substituting the factorial with a Γ-function, this will be useful later on, we find

$$|\Delta| = 4E_C\left(\frac{\eta}{2}\right)^{2q}\left(\frac{1}{\Gamma(2q)}\right)^2. \tag{3.4}$$

Note that Eq. (3.4) reproduces our result from Sec. 2.3 for the band gap between band one and two at $p = 1/2$ which in this case is identical to $q = 1/2$. For arbitrary q, we can already see that the band gap is inversely proportional to q^q because of the Γ-function. Therefore, the band gap decreases very quickly if we increase q which physically corresponds to considering higher band gaps. This observation will become important when we calculate the transition probability in the next section.

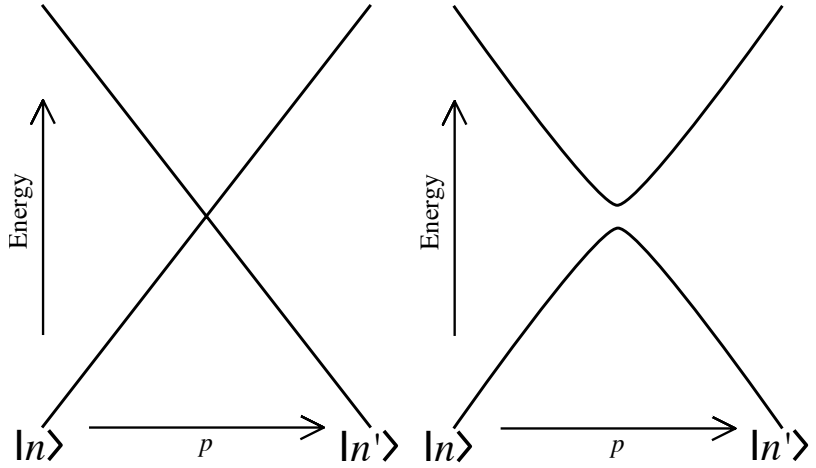

Figure 3.1: Energy of the two-level system as a function of the external parameter p. The left figure shows the unperturbed problem and the right figure the avoided crossing due to the finite gap from Eq. (3.4). The energy gap $\delta E(p) = E_n(p) - E_{n'}(p)$ between the two states varies with the external parameter p.

3.2 Landau-Zener approximation

The Landau-Zener approximation is a semi-classical approach to describe the transition probability between two states with an avoided crossing, see Fig. 3.1, when the energy splitting $\delta E = E_n - E_{n'}$ between the states varies linearly in time. We will use this approximation for our specific problem where a semi-classical charge state travels through the bands, that are split-up due to the Josephson energy E_J. Here, we can describe our problem with the external parameter p, see Fig. 3.2. But in order to use the Landau-Zener approximation with our new external parameter p, our band gap needs to vary linearly in p and p needs to vary linearly in time. Both conditions are generally not fulfilled. However, if we assume that we start with the charge $q_0 = n_0 + p_0$ far enough away from our crossing at $q = n + p$, we can approximate the velocity in the vicinity of the crossing as constant. If we now also approximate the underlying quadratic potential linearly in p at the same critical point, we fulfill the requirements to use the Landau-Zener approximation, which tells us that the transition probability can be written as [9]

$$P_{\mathrm{LZ}} = \exp\left(-2\pi \frac{|\Delta|^2}{d[\delta E(p)]/dt}\right). \tag{3.5}$$

Since we have already calculated Δ in the last section, we only need to calculate the derivative $d[\delta E(p)]/dt$ which we will write as $(d[\delta E(p)]/dp)\ (dp/dt) = v_E\, v_p$.

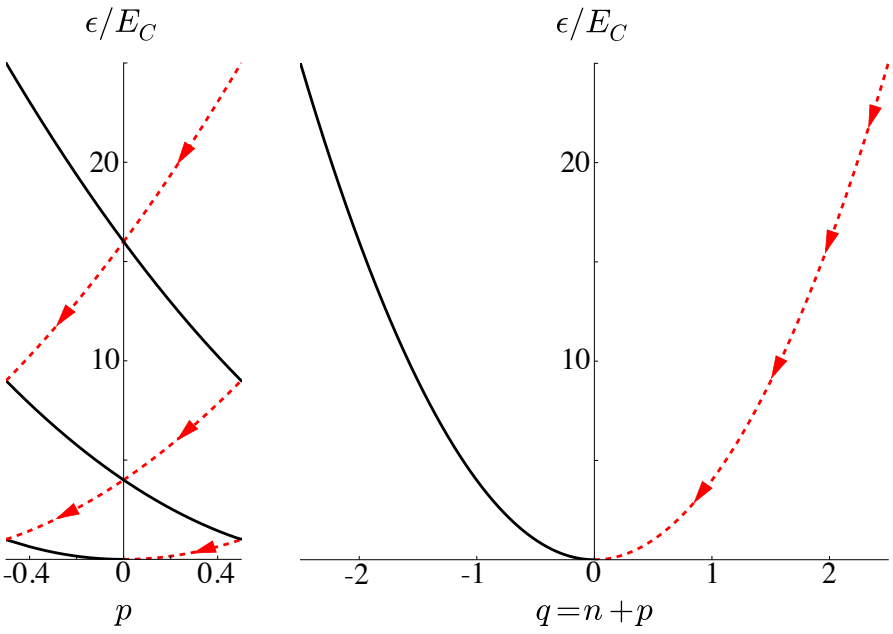

Figure 3.2: Tunneling process between bands in a reduced zone scheme (left) and an extended zone scheme (right). If we always tunnel at the avoided crossings, we can neglect the band gaps entirely and instead focus on the harmonic form of our potential in the extended zone scheme.

Now, we will use the Hamiltonian $\hat{H}$ in the limit $E_J = 0$

$$\hat{H}_{CL} = 4E_C(\hat{n}+p)^2 + \frac{1}{2}E_L\hat{\varphi}^2 = 4E_C\hat{q}^2 + \frac{1}{2}E_L\hat{\varphi}^2 \tag{3.6}$$

to approximate both velocities separately. The speed v_E, with which the energy gap varies in p, can be obtained by evaluating dE_{CL}/dp at the critical points $p = 0$ or $p = 1/2$ and multiplying the result by two, as the energy gap varies twice as fast as the energy of our state itself. Making use of the half-integer $q = n + p$ introduced in Eq. (3.6), the result can be written as $v_E = 16E_Cq$.

The speed v_p depends on the total energy of our system $E_0 = 4E_Cq_0^2$. Since φ has the properties of a momentum, we can write $v_p = dE_{CL}/d\varphi = E_L\varphi$. Now, we only have to evaluate φ at the critical point $q = n + p$. Knowing that $E_0 = E_{CL}$, we find

$$\varphi = \sqrt{\frac{8E_C}{E_L}}\sqrt{q_0^2 - q^2}. \tag{3.7}$$

At this point, it is important to remember that the Landau-Zener approximation assumes the velocity to remain constant while moving through the crossing. Therefore, we can not evaluate our probability at $q \approx q_0$ but instead have to

choose a q_0 far enough away from the crossing to be able to approximate our velocity as constant.

After these calculation, we can write the Landau-Zener transition probability as

$$P_{\mathrm{LZ}} = \exp\left(-\frac{\pi}{4}\sqrt{\frac{8E_C}{E_L}}\left(\frac{\eta}{2}\right)^{4q}\frac{1}{\Gamma(2q)^4}\ \frac{1}{q\sqrt{q_0^2-q^2}}\right). \tag{3.8}$$

It is already obvious that the transition probability becomes very small very quickly for large q due to the gamma function since $\Gamma(q) \sim q^q$. We now want to get a more precise understanding of the critical q^* which marks the charge at which the transition probability has decreased to $P_{\mathrm{LZ}} = 1/2$. We can approximate this charge by assuming

$$\sqrt{\frac{8E_C}{E_L}}\left(\frac{\eta}{2}\right)^{4q^*}\frac{1}{\Gamma(2q^*)^4}\ \frac{1}{q^*\sqrt{q_0^2-q^{*2}}} = 1 \tag{3.9}$$

and applying the logarithm on both sides of the equation using Stirling's formula to approximate the Γ-function. Only concentrating on the terms of highest order in q^* and using the substitution $\tau = \sqrt{8E_C/E_L}$, we can write

$$8q^*\ln\left(\frac{q^*}{\sqrt{\eta}}\right) = \ln(\tau). \tag{3.10}$$

To leading order, we can therefore find that $\ln(q^*) \sim \ln[\ln(\tau)]$ independent of η.

Another way of getting a better understanding of P_{LZ} and the critical q^* is to assume q to be a continuous variable and plot P_{LZ} for different τ and η. The results in Fig. 3.3 and 3.4 confirm our logarithmic proportionality between q^* and τ even for small q^*, although our small q^* is not independent of η but instead grows smaller with smaller η and therefore smaller band gaps. We can also see that q^* remains very small for realistic values of τ and η and Fig. 3.3 shows that P_{LZ} has a very steep curve at the critical q^*. This property is mostly due to the Γ-function and means that the transition probability changes very abruptly from approximately one to about zero in between transition points, where q is a half-integer.

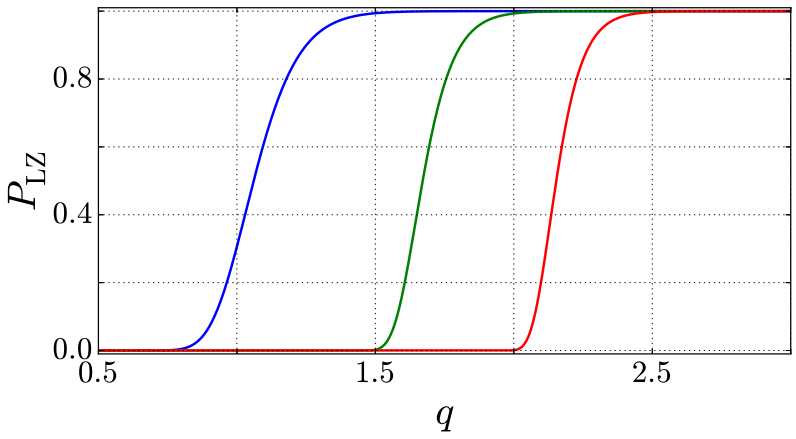

Figure 3.3: Tunneling probability P_{LZ} for $\eta = E_J/4E_C = 0.7$, initial charge $q_0 = 10$, and varying $\tau = \sqrt{8E_C/E_L}$. The blue line shows the tunneling probability for $\tau = 10^3$, the green line for $\tau = 10^6$, and the red line for $\tau = 10^9$. The curve of P_{LZ} becomes very steep around $P_{\mathrm{LZ}} = 1/2$.

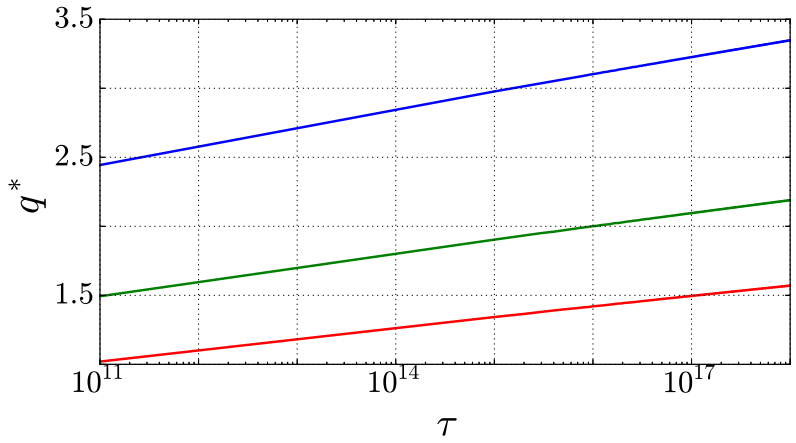

Figure 3.4: Logarithmic plot of the critical q^* with $P_{\mathrm{LZ}}(q^*) = 1/2$ dependent on $\tau = \sqrt{8E_C/E_L}$ with the initial charge $q_0 = 10$ and for three different $\eta = E_J/4E_C$. The blue line shows the critical q^* for $\eta = 0.7$, the green line for $\eta = 0.07$, and the red line for $\eta = 0.007$. The logarithmic dependency of q^* on τ is clearly visible and the critical q^* grows larger for larger η.

Because of these properties, we can distinguish two regimes in the tunneling process:

i) If we start at a sufficiently large q_0, we will always tunnel between bands up to q^*. Since q^* remains very small for realistic τ and η, due to the logarithmic proportionality, see Eq. (3.10), we can assume that we will tunnel down to the lowest band and therefore neglect E_J entirely in this regime. This reduces our problem to an harmonic oscillator, as we can see in Fig. 3.2.

ii) However, if we start with a $q_0 \lesssim q^*$, no tunneling between bands occurs as the transition probability decreases very quickly in between transition points. We can therefore reduce our problem to a single band structure since we will always stay within the same band.

The calculation of the tunneling probability now allows us to interpret the behavior of Ω. In Sec. 2.3, we concluded that $\Omega_{1,2}$ assumes the form of a δ-distribution for $\eta \to 0$. This statement is equivalent to the observation that the tunneling probability becomes one for $\Delta \to 0$. Intuitively speaking, $\Omega_{s,s'}(p)$ couples the two bands s and s' and if Ω assumes the form of a δ-distribution, the two bands are strongly coupled at one discrete point where tunneling occurs.

3.3 General properties of both regimes

In the last section, we introduced two separate regimes and the aim of this section is to discuss the general properties of both regimes. We will start with the first regime where tunneling between the bands is suppressed and we can thus consider only a single band. We now have a periodic potential in $q = n + p$ with periodicity one but while the lowest band still has an underlying quadratic potential the higher bands have a triangular form.

As long as our energy is small enough, such that we are not to close to the maxima of the potential, the states are confined to a single potential valley since the tunneling probability between the valleys scales exponentially with the width of the potential barrier. If we also take into account that the presence of the Josephson coupling smoothes the cusp of the triangular potential, we can describe the potential as

$$V(q) = \sqrt{\beta^2 q^2 + \alpha^2} \tag{3.11}$$

where q is measured from the valley of the potential and can not be larger than $1/2$, because we want to stay in one band.[2] However, the gradient β can be described with our previous half-integer q through $\beta = 8E_C q$ and α is half of the smallest band gap between the two adjacent bands and can therefore be identified with Δ.

In the second regime — the harmonic regime, where we can neglect E_J entirely — our Hamiltonian can be written as

$$\hat{H} = 4E_C\hat{q}^2 + \frac{1}{2}E_L\hat{\varphi}^2. \tag{3.12}$$

Using the ladder operators, we can make the substitution

$$\hat{q} = \left(\frac{E_L}{32E_C}\right)^{\frac{1}{4}}(\hat{a}^\dagger + \hat{a}) \quad \text{and} \quad \hat{\varphi} = i\left(\frac{2E_C}{E_L}\right)^{\frac{1}{4}}(\hat{a}^\dagger - \hat{a}) \tag{3.13}$$

to transform our Hamiltonian into the form

$$\hat{H} = \sqrt{8E_C E_L}\left(\hat{a}^\dagger\hat{a} + \frac{1}{2}\right) \quad \text{with} \quad E_m = \sqrt{8E_C E_L}\left(m + \frac{1}{2}\right). \tag{3.14}$$

If we now compare our Hamiltonian to the Hamiltonian $\hat{H}_{\text{ho}}$ of the harmonic oscillator with mass m and frequency ω

$$\hat{H}_{\text{ho}} = \frac{\hat{p}^2}{2m} + \frac{1}{2}m\omega^2\hat{x}^2, \tag{3.15}$$

we can identify the mass $m = (E_L)^{-1}$ and the plasma frequency $\omega = \sqrt{8E_C E_L}/\hbar$. Since our frequency is small in the limit $E_L \ll 8E_C$, we can use the semi-classical approximation for our following calculations. With this information, we can now start to analyze time scales of charge relaxation in both regimes in the next chapters.

[2] Basically, this means that $q = p$ and we are back in the reduced band scheme from Fig. 3.2

Chapter 4

Time-scales of a wave packet

4.1 General structure and dispersion

In this chapter, we will begin with a Gaussian wave packet prepared at an initial charge q_0 with width σ and then observe its time evolution. We are especially interested in the case $\sigma\tau^{1/2} \ll 1$, with $\tau = \sqrt{8E_C/E_L}$, since we want to start with a strongly localized charge on the superconducting island.

To get a better understanding of the general structure of our problem, we take a closer look at the second regime where we can assume E_J to be zero and therefore use the Hamiltonian in Eq. (3.14) for our calculations. Here, the time dependent probability density can be written as

$$\begin{aligned} |\Psi(q)|^2 &= \sqrt{\frac{1}{\pi k_{\mathrm{qm}}}} \exp\left(-\frac{k_{\mathrm{cl}}}{k_{\mathrm{qm}}}\right) \\ \text{with} \quad k_{\mathrm{cl}} &= [q - q_0 \cos(\omega t)]^2 \\ \text{and} \quad k_{\mathrm{qm}} &= \frac{1}{\tau^2\sigma^2}\left[\sin^2(\omega t) + \tau^2\sigma^4\cos^2(\omega t)\right], \end{aligned} \tag{4.1}$$

see App. B, with $\tau = \sqrt{8E_C/E_L}$ and $\omega = \sqrt{8E_C E_L}/\hbar$ defined in the previous chapter. Here, we can see that our problem contains two time scales: The first one is the classical time scale dependent on the classical equation of motion of the harmonic oscillator that is visible in the numerator k_{cl} of the exponential function. The second time scale is due to the quantum mechanical dispersion of the wave packet and is visible in the denominator k_{qm} of the exponential function.

While the classical time scale is strongly dependent on the potential and there-

fore the regime that we are in, the quantum mechanical scale is independent of the specific regime in our limit of a strongly localized charge at $t_0 = 0$ and with $\omega t \ll 1$. In this limit, our scale describes the dispersion of a free wave packet and is therefore independent of the specific potential our charge is in. If we take a closer look at k_{qm} in those limits, we find that the dispersion time scale that we define by the time when $k_{qm} = 1$ can be written as

$$t_{qm} = \frac{\hbar\sigma}{E_L} \tag{4.2}$$

independently of the scale E_C describing our quadratic potential. We will now use the re-substitution $q \to n + p$ to separate the discrete charge from the continuous Bloch momentum in the probability density, see Sec. 3.3. Taking a closer look at the diagonal elements of the reduced density matrix $\varrho(p, p')$, which physically corresponds to the probability density at a certain Bloch momentum p independent of the discrete charge n, we find

$$\varrho(p, p) = \vartheta[-p + q_0\cos(\omega t); ik_{qm}\pi], \tag{4.3}$$

see App. B, where ϑ represents the classical Jacobi theta function [10]. Here, we can recognize the same two time scales as before. The plot in Fig. 4.1 shows the diagonal elements of the reduced density matrix at different times and we can clearly see both of our scales: The classical time scale responsible for the movement of the maximum of the wave packet and the quantum mechanical scale causing its increasing width. The figure also shows that our chosen time scale t_{qm} represents the dispersion time very well as the wave packets are depicted at equally spaced times $t \in [0, t_{qm}/2]$ and we can clearly see that the wave packet has mostly smeared out after that time.

After calculating both time scales in the harmonic regime and establishing that the quantum mechanical scale is independent of the regime in our specific limits, we only need to take a better look at the classical time scale in our single band regime to complete this chapter.

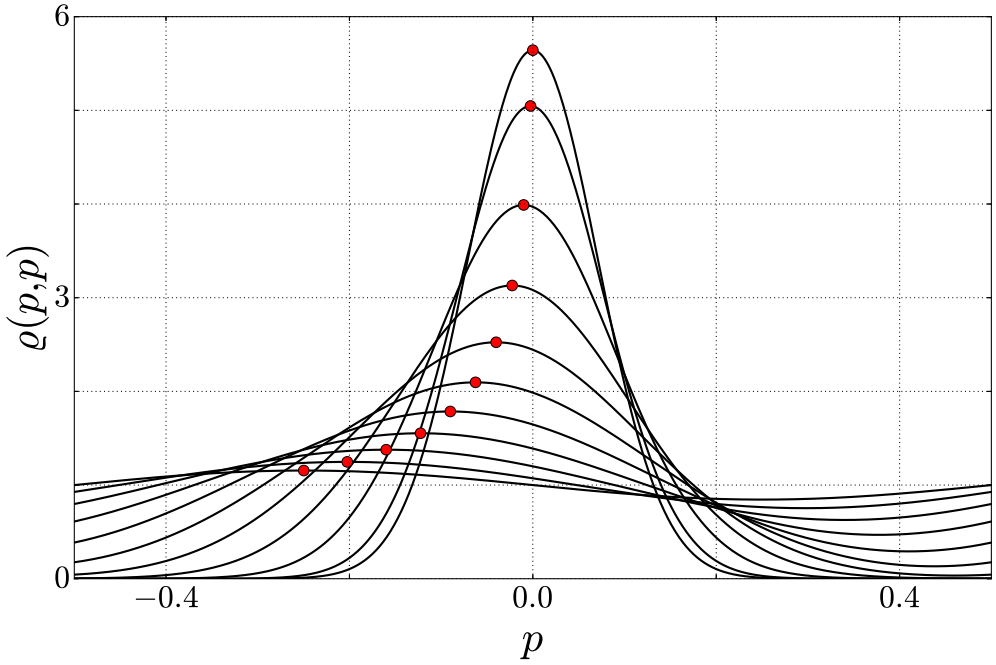

Figure 4.1: Reduced density matrix $\varrho(p,p)$ at different, equally spaced times $t \in [0, t_{qm}/2]$ with the initial charge $q_0 = 50$, $\tau = \sqrt{8E_C/E_L} = 2$, and the width of the wave packet $\sigma = 0.1$. The red dots mark the maxima of the wave packets. The classical time scale is visible in the movement of the maximum of the wave packet while the quantum mechanical scale causes the increasing width of the wave packet.

4.2 Classical time scale of the single band regime

The aim of this section is to get a better understanding of the classical time scale in the single band regime. We will only consider the case $\alpha = 0$ since this is a very accurate assumption for the upper bands. With the Lagrangian

$$\mathcal{L} = \frac{\dot{q}^2}{2E_L} - \beta|q|, \tag{4.4}$$

the equation of motion for our charge can be written as

$$\ddot{q} = \mp\beta E_L. \tag{4.5}$$

Now, we can solve the equation of motion with the boundary conditions $q(t{=}0) = q_0$ and $\dot{q}(t{=}0) = 0$ and get a motion with periodicity $T = 4\sqrt{2q_0/E_L\beta}$. In the first fundamental period, the solution assumes the form

$$q(t) = \begin{cases} -\frac{1}{2}E_L\beta t^2 + q_0, & \text{for } t \in [0, \frac{T}{4}), \\ \frac{1}{2}E_L\beta t^2 - \frac{1}{2}\sqrt{2E_L\beta q_0}t + 3q_0, & \text{for } t \in [\frac{T}{4}, \frac{3T}{4}), \text{ and} \\ -\frac{1}{2}E_L\beta t^2 + \sqrt{2E_L\beta q_0}t - 15q_0, & \text{for } t \in [\frac{3T}{4}, T). \end{cases} \tag{4.6}$$

Figure 4.2 shows both the motion in an harmonic oscillator and the motion in the triangular potential. The difference between both is very small as long as they have the same periodicity T. The main distinction however is the dependency of T on q_0. The periodicity of a harmonic oscillator does not depend on the initial charge because it is independent of the energy of the system while the periodicity T of our single band structure is proportional to $\sqrt{q_0}$ as our potential has no longer the form of an harmonic oscillator even if the classical motions still look very similar. We will come back to this property and its implications for the quantum mechanical energy levels in the next chapter.

Another difference is visible if we take a closer look at the momentum $\varphi(t)$ in Fig. 4.3. Here, we can see that the non-analyticity of our potential is transferred to the momentum. This and additional properties of the momentum will also be further discussed in the next chapter.

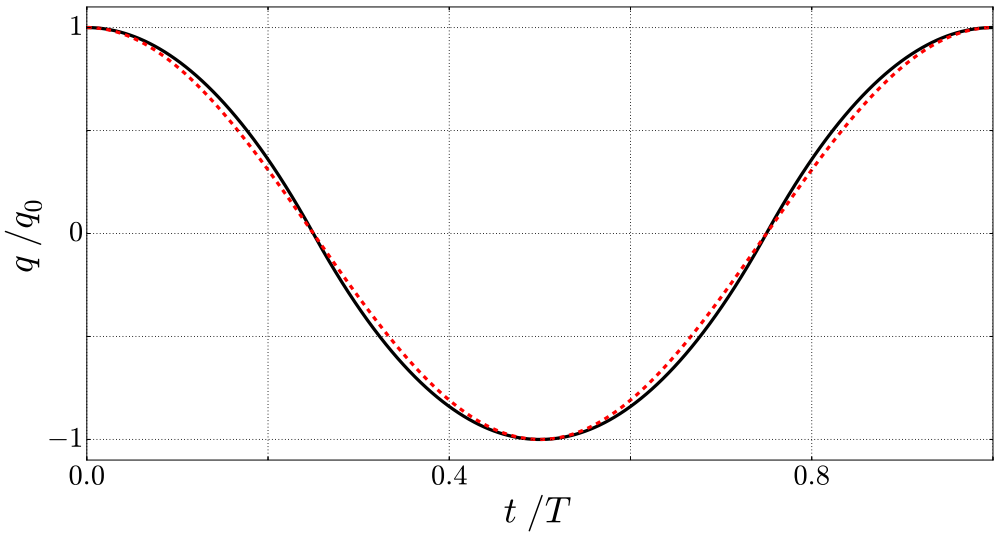

Figure 4.2: Classical motion of a charge q in the harmonic regime with $q = q_0 \cos(2\pi t/T)$ (red, dashed) and the single band regime with the band gap $\alpha = 0$ (black). Both motions have the periodicity T and initial charge q_0 and are smooth and very similar.

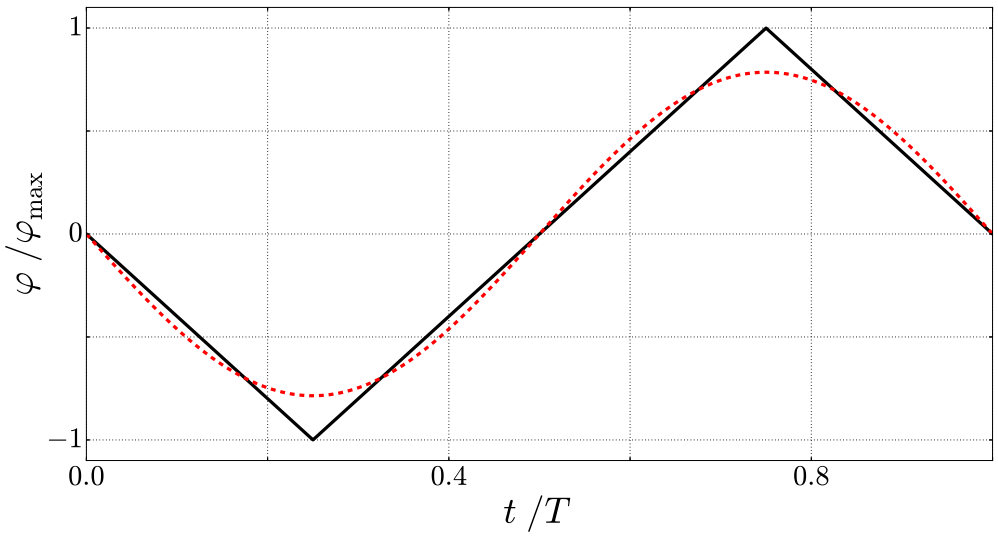

Figure 4.3: Momentum φ of a charge in the harmonic regime (red, dashed) and the single band regime for the band gap $\alpha = 0$ (black), in units of maximal momentum of the motion in the single band regime $\varphi_{\max}$. Both motions have periodicity T and initial charge q_0. The momentum of the charge in the harmonic regime is analytic, while the momentum in the single band regime is non-analytic for $\alpha = 0$.

Chapter 5

Perturbation by charge noise

5.1 General calculations

While the last chapter focused on the time scales of specially prepared wave packets, this chapter will concentrate on time scales that are due to a time-dependent perturbation. For this, we will take a closer look at our Hamiltonian in Eq. (2.3). Up until now, we always assumed the offset charge $n_g = V_g C_g/2e$ to be a constant but from now on we will look at $n_g = n_g(t)$. This will in general be the case as the perturbation can be due to charge noise or other external influences. We will simulate our perturbation using the function

$$n_g(t) = \frac{C_g}{2e}\left[(V_f - V_i)\left(\frac{\arctan(\mu t)}{\pi} + \frac{1}{2}\right) + V_i\right] \tag{5.1}$$

which regulates the voltage, starting at V_i and ending at V_f, on the time scale of μ. Our aim is to calculate the transition probability $P_{f,i}$ between two energy eigenstates $|i\rangle$ and $|f\rangle$ of an undisturbed Hamiltonian $\hat{H}_0$ using time-dependent perturbation theory

$$\begin{aligned} P_{f,i} &= \left|\int_{-\infty}^{\infty} dt\, \langle f|\, \dot{n}_g(t)\hat{\varphi}\, |i\rangle\, e^{i\Delta E t/\hbar}\right|^2 \quad \text{with} \quad \Delta E = E_f - E_i \\ &= |\langle f|\, \hat{\varphi}\, |i\rangle|^2 \left|\int_{-\infty}^{\infty} dt\, \dot{n}_g(t)\, e^{i\Delta E t/\hbar}\right|^2 \\ &= |\langle f|\, \hat{\varphi}\, |i\rangle|^2 \left(\frac{C_g}{2e}\right)^2 (V_f - V_i)^2\, e^{-2|\Delta E/\hbar\mu|}. \end{aligned} \tag{5.2}$$

After evaluating the integral, we only have to calculate the matrix elements $\langle f|\, \hat{\varphi}\, |i\rangle$. The calculation of these matrix element in both regimes will be the subject of the next sections.

5.2 Adiabatic scale in the harmonic regime

For the calculation of the matrix element $\langle f|\,\hat{\varphi}\,|i\rangle$ in the harmonic regime, we can use Eq. (3.13) and the properties of the ladder operator to find

$$\langle m'|\,\hat{\varphi}\,|m\rangle = i\left(\frac{2E_C}{E_L}\right)^{\frac{1}{4}}\left(\sqrt{m'+1}\,\delta_{m',m-1} - \sqrt{m'}\,\delta_{m',m+1}\right). \tag{5.3}$$

Therefore, only transitions to adjacent energy levels are possible. We can now easily calculate the total transition probability from state m to any state

$$\begin{aligned} P_m = \sum_{m'\neq m} P_{m',m} &= \left(\frac{C_g}{2e}\right)^2 (V_f - V_i)^2\, e^{-\frac{2\sqrt{8E_CE_L}}{\hbar\mu}} \sqrt{\frac{2E_C}{E_L}}(2m+1) \\ &= \frac{E_m}{E_L}\left(\frac{C_g}{2e}\right)^2 (V_f - V_i)^2\, e^{-\frac{2\sqrt{8E_CE_L}}{\hbar\mu}} \end{aligned} \tag{5.4}$$

where E_m is the initial energy of the charge at $t = -\infty$. From this result, we can gather that whether we tunnel or not is strongly dependent on the ratio of $\omega = \sqrt{8E_CE_L}/\hbar$ to μ. In the regime $\mu \ll \omega$ a transition is very unlikely since the energy scale of the perturbation is small compared to the energy gap between two energy levels. The contrary is the case for $\mu \gg \omega$. Here, transition is very likely because the energy scale of the perturbation is large enough to make crossing from one state to another energetically possible. In order to suppress transition, it is therefore necessary to have μ smaller than the adiabatic time scale set by the plasma frequency ω.

5.3 Additional scale in the single band regime

For the single band regime, we will use semi-classical methods to calculate our matrix element. We start by assuming the case $\alpha = 0$ for our potential $V(q) = \sqrt{\beta^2q^2 + \alpha^2}$ and calculate the level spacing using Bohr-Sommerfeld quantization. Here, the quantized energy can be calculated via [7]

$$m + \frac{1}{2} = \frac{1}{2\pi}\oint \sqrt{\frac{2}{E_L}\left[E_m - V(q)\right]}\,dq \tag{5.5}$$

and we obtain the result

$$E_m = \left[\frac{3\pi}{4}\sqrt{\frac{E_L}{2}}\beta\left(m+\frac{1}{2}\right)\right]^{\frac{2}{3}}. \tag{5.6}$$

Since we can approximate the level spacing ΔE_m via

$$\frac{dE_m}{dm} \approx \frac{E_{m+1} - E_m}{1} = \Delta E_m, \tag{5.7}$$

we find that $\Delta E_m = 2\pi/T_m$ if we use our definition of the period $T = 4\sqrt{2q_0/E_L\beta}$ of the classical motion in the triangular potential from Sec. 4.2 which depends on q_0 and thus the energy level m. This shows the connection between the classical period T and the energy spacing in the semi-classical limit and explains why the energy levels of a harmonic oscillator are equally spaced while this is no longer the case for the triangular potential. Only for a harmonic potential, the period T is independent of energy which translates to energy-independent level spacing.

Now, the correspondence principle states that our matrix elements can be approximated via the Fourier transformation [7]

$$\langle m + \Delta m| \hat{\varphi} |m\rangle = \frac{1}{T_m} \int_0^{T_m} dt\, \varphi(t) e^{i\Delta E_m \Delta m t}, \tag{5.8}$$

where $\varphi(t)$ is the classical time dependent momentum of our system. If we use Eq. (4.6) and the relation $\varphi(t) = \dot{q}(t)/E_L$, we find

$$\langle m + \Delta m| \hat{\varphi} |m\rangle = \begin{cases} i\beta T_m \frac{1}{\pi^2 \Delta m^2}, & \text{for } \Delta m \text{ uneven and} \\ 0, & \text{for } \Delta m \text{ even} \end{cases} \tag{5.9}$$

in the limit $\alpha = 0$. Here the purely imaginary components are due to our momentum being an odd function of time and we can now calculate the total transition probability

$$\begin{aligned} P_m &= \sum_{\Delta m \neq 0} P_{m+\Delta m, m} \\ &= \frac{8\beta^2}{\Delta E_m^2 \pi^2} \left(\frac{C_g}{2e}\right)^2 (V_f - V_i)^2 \sum_{j=0}^{\infty} \frac{e^{-2(2j+1)\Delta E_m/\hbar\mu}}{(2j+1)^4} \\ &= \frac{8\beta^2}{\Delta E_m^2 \pi^2} \left(\frac{C_g}{2e}\right)^2 (V_f - V_i)^2 \chi_4\left(e^{-2\Delta E_m/\hbar\mu}\right) \end{aligned} \tag{5.10}$$

with $\chi_4(x)$ representing the fourth Legendre χ-function. As we can see in Fig. 5.1, $\chi_4(x)$ can be approximated as x. Besides considering the graph, there is also an intuitive way to understand this approximation.

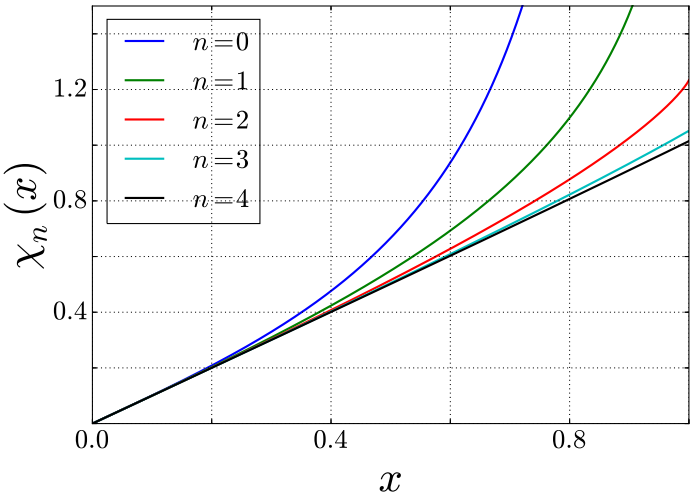

Figure 5.1: Plot of different Legendre χ-functions $\chi_n(x)$. It is obvious that $\chi_4(x)$ can be approximated very well via $\chi_4(x) \approx x$.

If we take a closer look at our sum in Eq. (5.10), we can make out two different cases:

- Either, the exponent $\Delta E_m/\hbar\mu$ is very large and we therefore only need to consider the first term $j = 0$ of the sum
- or the exponent is very small and we can neglect the scale on which the exponent varies compared to the polynomial. Then, we can evaluate the exponent at $j = 0$ and only have to calculate the sum

$$\sum_{j=0}^{\infty} \frac{1}{(2j+1)^4} = \frac{\pi^4}{96} \approx 1. \tag{5.11}$$

Therefore, our final result can be written as

$$P_m = \frac{8\beta^2}{\Delta E_m^2 \pi^2} \left(\frac{C_g}{2e}\right)^2 (V_f - V_i)^2 \, e^{-2\Delta E_m/\hbar\mu} \tag{5.12}$$

which holds both for $\Delta E_m/\hbar\mu \ll 1$ and $\Delta E_m/\hbar\mu \gg 1$ and again depends only on the adiabatic parameter $\Delta E_m/\hbar\mu$.

Having considered the case $\alpha = 0$, we now want to take a closer look at the case $\alpha \neq 0$. Up to now, we took the Fourier transform of a non-analytic function and our Fourier coefficients decreased with $1/\Delta m^2$. However, if we add α to our calculation, the momentum becomes analytic and the Fourier coefficients will decrease exponentially as stated in the Paley-Wiener theorem [8]. Therefore,

we have neglected an additional exponential scale by neglecting α.

Since we can not calculate the equation of motion analytically for $\alpha \neq 0$, we need to find a way to approximate our momentum by using the relation $\varphi(q) = \sqrt{2\left[E - V(q)\right]/E_L}$. Because we are mainly interested in reproducing the properties of the momentum at $q = 0$, as the Fourier transformation is dominated by our nearly non-analytic point, we can make the approximation

$$\varphi(q) = \sqrt{\frac{2}{E_L}\left[E - V(q)\right]} \approx \sqrt{\frac{2E}{E_L}}\left(1 - \frac{V(q)}{2E}\right). \tag{5.13}$$

Since the Fourier transformation of a constant is a δ-distribution centered around zero, we can discard the constant offset because the matrix element of the momentum at $\Delta m = 0$ is not of interest to us. In order to get an expression for $\varphi(t)$, we approximate the speed at the cusp $q = 0$ because this point dominates our Fourier transformation. We therefore write $q \approx v_0 t$ with v_0 calculated via the relation $E(q_0) = E(0)$ as

$$v_0 = \sqrt{2E_L\left(\sqrt{\beta^2 q_0^2 + \alpha^2} - \alpha\right)}. \tag{5.14}$$

Now, we only have to calculate the Fourier transform, see Eq. (5.8), of $\widetilde{V}(t) = V(v_0 t)$. However, since our potential diverges for $|q| \to \infty$, due to our approximation in Eq. (5.13), we will take the Fourier transformation of the second derivative

$$\ddot{\widetilde{V}}(t) = \frac{\beta^2 v_0^2}{\sqrt{\alpha^2 + \beta^2 t^2 v_0^2}} - \frac{\beta^4 t^2 v_0^4}{\left(\alpha^2 + \beta^2 t^2 v_0^2\right)^{3/2}}, \tag{5.15}$$

which converges for $|q| \to \infty$, and multiply our result by $-1/\Delta m^2 \Delta E_m^2$ to calculate the transformation of our original function. With this information, our matrix element $\varphi_m(\Delta m) = \langle m + \Delta m | \hat{\varphi} | m \rangle$ can be calculated as

$$\begin{aligned} |\varphi_m(\Delta m)| &= \frac{1}{T_m}\sqrt{\frac{1}{2E_L E_m}}\frac{1}{\Delta m^2 \Delta E_m^2}\int_{-\infty}^{\infty} e^{i\Delta E_m \Delta m t}\,\ddot{\widetilde{V}}(t)dt \\ &= \sqrt{\frac{1}{2E_L E_m}}\frac{\alpha}{\pi|\Delta m|}K_1\left(\frac{|\Delta m \Delta E_m|\,\alpha}{\beta v_0}\right) \end{aligned} \tag{5.16}$$

with the Macdonald function $K_1(x)$ that has an asymptotic behavior of the form

$$\begin{aligned} K_1(x) &\xrightarrow{x\gg 1} \sqrt{\frac{\pi}{2}}\frac{e^{-x}}{\sqrt{x}} \quad \text{and} \\ K_1(x) &\xrightarrow{x\ll 1} \frac{1}{x}. \end{aligned} \tag{5.17}$$

First, we will use this asymptotic behavior to go back to our previous case $\alpha \to 0$ and find that we were able to reproduce our result from Eq. (5.9) as long as we multiply our result with the coefficient two. This coefficient is most likely due to our approximation in Eq. (5.13) because we assume here that we only have one cusp smoothed by α in our entire period while in reality we have two such cusps per period, which causes the additional factor. With this coefficient, we can approximate our matrix element for $|\Delta m| \gg \beta v_0/\Delta E_m \alpha$ as

$$|\varphi_m(\Delta m)| = \sqrt{\frac{\alpha\beta v_0}{\pi E_L E_m \Delta E_m}}\frac{1}{|\Delta m|^{3/2}} e^{-|\Delta m \Delta E_m|\alpha/\beta v_0}. \tag{5.18}$$

Before we take a closer look at this result, we will back up our calculation and assumptions by calculating the Fourier transformation numerically.

We start by calculating the integral

$$t(q) = \int_0^q \frac{1}{E_L \varphi(q')} dq', \quad q \in [0, q_0] \tag{5.19}$$

but to increase our numerical accuracy, we rewrite the momentum as

$$\varphi(q) = \sqrt{\frac{2}{E_L}}\sqrt{\frac{E^2 - V(q)^2}{E + V(q)}} = \sqrt{\frac{2}{E_L}}\sqrt{\frac{\beta^2(q_0^2 - q^2)}{E + V(q)}} \tag{5.20}$$

and use the substitution $y = \sqrt{q_0 - q}$. This helps us avoid the divergence at $q = q_0$ but it is also useful to avoid subtracting the two large but nearly identical numbers E and $V(q \approx q_0)$ from each other, which causes numerical problems. We then calculate $t(y)$ and numerically approximate the inverse function $y(t)$ for one quarter of a period. Now, we can already calculate $\varphi(t)$ by using Eq. (5.20) and re-substituting $q = q_0 - y(t)^2$. Then, the result for an entire period can be obtained by exploiting the symmetries of our problem.

Now, we can calculate the discrete Fourier transformation in Δm. The resulting function is only non-zero for uneven Δm just as our analytic result was for $\alpha = 0$. This is due to the symmetries of our momentum which we already

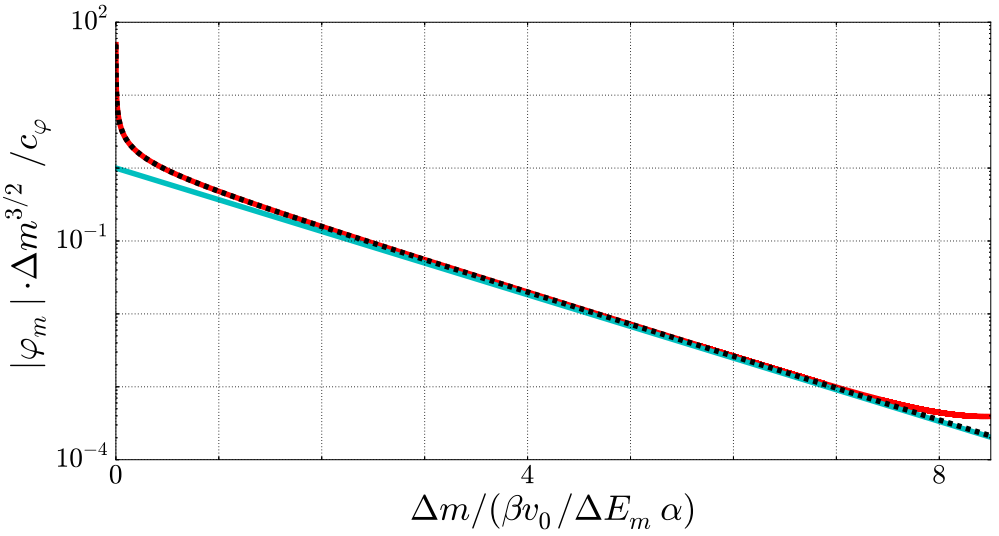

Figure 5.2: Plot of the Fourier transformation of the momentum for uneven Δm multiplied by $\Delta m^{3/2}$ in units of $c_\varphi = \sqrt{\alpha\beta v_0/\pi E_L E_m \Delta E_m}$, see Eq. (5.18): numeric calculation with $N = 2^{16}$ points in t (red), our asymptotic approximation for $|\Delta m| \gg \beta v_0/\Delta E_m \alpha$ (blue), and our analytic result in form of the Bessel function (black, dashed) with the energy scales $\alpha/E_L = 10^{-3}/2$ and $\beta/E_L = 1/2$ and the initial charge $q_0 = 3$. The asymptotic approximation works well for large Δm and the Bessel function reproduces our numeric result very well. The deviation between the Bessel function and the numeric calculation for very large Δm is due to the discrete Fourier transformation.

used to obtain an result for our momentum for an entire time period. If we now multiply our result by $\Delta m^{3/2}$ in order to obtain only the exponential dependency of the Fourier transformation for large Δm and compare our result to our analytic calculation and approximations, we obtain the results in Fig. 5.2 and 5.3. Since we used a discrete Fourier transformation, we have to keep in mind that our result is only equivalent to the analytic result for $\Delta m/N \ll 1$, where N is the amount of points in t we used for our transformation. This deviation is visible in our numerical calculation for very large Δm. However, we can clearly see that our numeric calculations are able to reproduce our analytic result and that the approximations in Eq. (5.17) are both very accurate in their regimes depending on the size of $\Delta m \Delta E_m \alpha/\beta v_0$.

We were therefore able to discover a second exponential scale in addition to the adiabatic scale in Eq. (5.12). To calculate the total transition probability

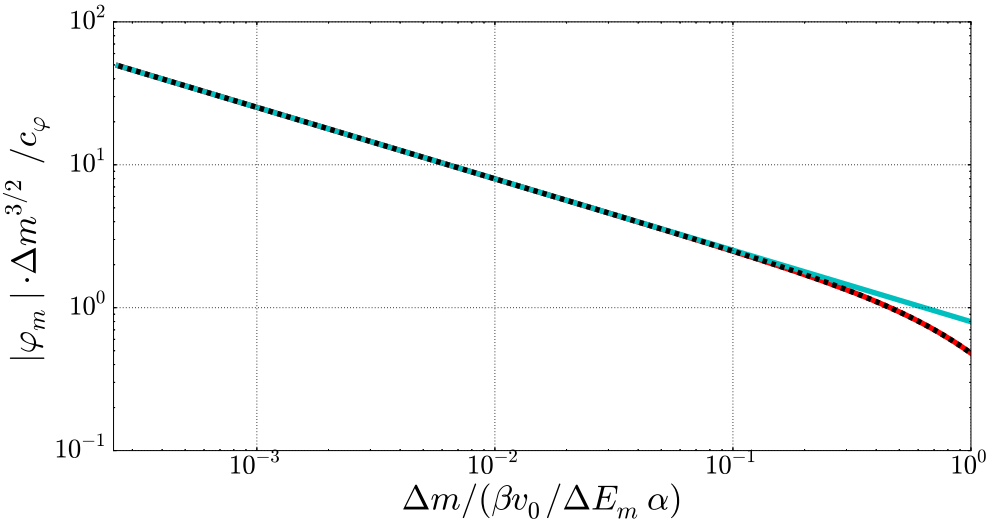

Figure 5.3: Plot of the Fourier transformation of the momentum for uneven Δm multiplied by $\Delta m^{3/2}$ in units of $c_\varphi = \sqrt{\alpha\beta v_0/\pi E_L E_m \Delta E_m}$, see Eq. (5.18): numeric calculation with $N = 2^{16}$ points in t (red), our approximation for $|\Delta m| \ll \beta v_0/\Delta E_m \alpha$ (blue), and our analytic result in form of the Bessel function (black, dashed) with the energy scales $\alpha/E_L = 10^{-3}/2$ and $\beta/E_L = 1/2$ and the initial charge $q_0 = 3$. The asymptotic approximation works well for small Δm and the Bessel function reproduces our numeric result very well.

defined by the sum

$$P_m = \frac{2\alpha^2}{E_L E_m \pi^2} \left(\frac{C_g}{2e}\right)^2 (V_f - V_i)^2 \cdot \sum_{\Delta m \neq 0} \frac{1}{\Delta m^2} K_1 \left(\frac{|\Delta m \Delta E_m| \, \alpha}{\beta v_0}\right)^2 e^{-2|\Delta m \Delta E_m/\hbar\mu|}, \tag{5.21}$$

we will use the same methods we used before to acquire Eq. (5.12) including our approximation $\pi^4/96 \approx 1$ from Eq. (5.11). The only difference is that we now have to divide our problem into two regimes depending on which approximation we want to use for our Bessel function. We also have to consider that again only uneven Δm form a contribution to our sum as we were able to see in our numeric calculations. For both regimes we then find

$$\begin{aligned} \frac{\Delta E_m \alpha}{\beta v_0} \ll 1: \;\; P_m &= \frac{4\beta^2 v_0^2}{E_L E_m \Delta E_m^2 \pi^2} \left(\frac{C_g}{2e}\right)^2 (V_f - V_i)^2 \, e^{-2\Delta E_m/\hbar\mu}, \\ \frac{\Delta E_m \alpha}{\beta v_0} \gg 1: \;\; P_m &= \frac{2\beta v_0 \alpha}{E_L E_m \Delta E_m \pi} \left(\frac{C_g}{2e}\right)^2 (V_f - V_i)^2 e^{-2\Delta E_m/\hbar\mu'}, \end{aligned} \tag{5.22}$$

with $1/\mu' = 1/\mu + \hbar\alpha/\beta v_0$. We can see that for $\Delta E_m \alpha/\beta v_0 \gg 1$ a second exponential scale was added to our solution. Therefore, we now have to compare our level splitting not only to the time scale of our perturbation but also to a second scale depending on the form of our potential. The new μ' is dominated by this scale for $\mu \gg \beta v_0/\hbar\alpha$.

In order to get a better understanding of how this new scale depends on our energy scales E_L, E_J, and E_C, we rewrite our expression using the approximation $\Delta E_m = 2\pi/T_m \approx \pi\sqrt{E_L\beta/8q_0}$ for $\alpha = 0$. This approximation is justified because the period T_m is dominated by the motion at the turning point q_0, which is far away from the regime effected by α. We can therefore write

$$\begin{aligned}\frac{\Delta E_m \alpha}{\beta v_0} &= \frac{\pi\left(\frac{E_J}{8E_C}\right)^{2q}\frac{1}{\Gamma(2q)^2}}{\sqrt{32q_0q\left(\sqrt{4q^2q_0^2+\left(\frac{E_J}{8E_C}\right)^{4q}\frac{1}{\Gamma(2q)^4}}-\left(\frac{E_J}{8E_C}\right)^{2q}\frac{1}{\Gamma(2q)^2}\right)}} \\ &= \frac{\pi f(\eta,q)}{\sqrt{32q_0q\left(\sqrt{\frac{4q_0^2q^2}{f(\eta,q)^4}+1}-1\right)}} \quad \text{with } f(\eta,q)=\frac{\left(\frac{\eta}{2}\right)^q}{\Gamma(2q)},\end{aligned} \tag{5.23}$$

where q is again a half-integer denoting the band we are in and $q_0 < 1/2$ indicates our initial charge in that particular band. Our scale is independent of E_L and only $\eta = E_J/4E_C$ and the band denoted by q are important for the size of our scale. Since $f(\eta, q) \to 0$ for $q \to \infty$ independent of η, our exponent $\Delta E_m \alpha/\beta v_0 \to 0$ for large q. This means that our new exponential scale is solely important in lower bands.

If we stay in those lower bands, we can reduce our total transition probability by increasing $f(\eta, q)$. The only way to do that is to increase η and since large η and small q are both conditions that promote our single band regime, see Sec. 3.2, we are actually able to assume this particular limit. Our system can therefore be protected against time-dependent perturbation independently of the adiabatic scale for $E_J \gg 4E_C$.

5.4 Plasma frequencies and screening

This section focuses on a classical interpretation of our result. Therefore, we will take a closer look at the plasma frequency of the inductively shunted CPB. But first, we will discuss the connection between the plasma frequency of a

system and the system's ability to screen charges.

From the outside, a free electron gas is electrically neutral and if for example a positive charge is added to a free electron gas, the electrons will surround the charge screening the environment from the effects of the positive charge. Here, the Debye length $\lambda_D = \sqrt{\varepsilon_0 k_B T/\rho e^2}$ is the measure of how far the electrostatic effects due to the additional charge persist [2].[1] If our perturbation becomes dynamic, we have to compare the frequency of the perturbation to the frequency with which charges are able to move around in our system. This frequency is the plasma frequency of our system. If the frequency of the perturbation is smaller than the plasma frequency, the free charge carriers of the system are able to "keep up" with the motion of the test charge. In this case, the system is able to screen the charge. If the opposite is the case, the charge carriers of the system are too slow and the screening becomes imperfect

In the harmonic regime, where we neglect the influence of the Josephson junction entirely and therefore only have to consider an LC-resonator, the plasma frequency is $\omega_{LC} = \sqrt{8E_C E_L}/\hbar$. Here, we have to compare the frequency of the perturbation to ω_{LC} if we want to know whether we can screen our system from charge noise. This statement is equivalent to our result from Sec. 5.2, where we calculated that the transition probability depends only on the adiabatic scale.

In the limit of a large Josephson energy, the influence of the inductance can be neglected. However, since the Josephson junction behaves mainly like an inductance,[2] the plasma frequency in this particular limit is $\omega_{JC} = \sqrt{8E_C E_J}/\hbar$. This frequency becomes very large in the limit $E_J \gg 4E_C$ screening our circuit from charge noise.

[1] In this formula, ε_0 denotes the electric constant, k_B the Boltzmann constant, T the temperature, ρ the charge density, and e the elementary charge.

[2] We can easily see this by approximating $1 - \cos(\varphi) \approx \varphi^2/2$ in our Hamiltonian.

Chapter 6

Conclusion

This thesis has dealt with the topic of charge relaxation in a superconducting island via an inductive shunt. In Ch. 2. the general properties of the Hamiltonian of the inductively shunted CPB were examined with regards to the Hamiltonian's properties in the Bloch wave base. Then, the transition probability between charge bands formed due to the Josephson energy were calculated in Ch. 3. Here we were able to separate our problem into two regimes: In the first regime, where the Josephson energy causing the band splitting could be neglected entirely, the inductively shunted CPB could be understood as an LC-resonator. In the second regime, where no tunneling between bands occurred, we only had to consider a single charge band whose form depended on the band index and the ratio E_J/E_C. After establishing both regimes, we began to look at general properties of charge relaxation time scales in our circuit.

We started by preparing a wave packet at an initial charge q_0 with width σ and observing its time evolution in Ch. 4, discovering two different time scales: The first scale was due to the quantum mechanical dispersion of the wave packet. This scale was identical for both of our regimes in the limit of a strongly localized charge at t_0 and a large inductance $E_L \ll E_C$, as this limit reproduced the dispersion time scale of a free particle with $t_{qm} = \hbar\sigma/E_L$. The second time scale corresponded to the classical movement of the charge in the circuit and therefore depended on the different potentials in our regimes.

All these calculations enabled us to calculate transition probabilities between eigenstates caused by a time-dependent perturbation due to charge noise in Ch. 5 of this thesis. Here, we used semi-classical methods to discover that the total transition probability in the LC-resonator and also in our single band regime for small E_J/E_C depended only on driving frequencies in the adiabatic

regime. This meant that we had to compare the frequency of our perturbation to the level spacing of our system if we wanted to know whether a transition occurs or not.

However, in the case of a high ratio between E_J and E_C, our transition probability is dominated by a second exponential scale which protects our system against transitions independent of the adiabatic scale. Therefore, one could say that high Josephson energies render our circuit insensitive to charge noise. In this particular case, we should not compare the frequency of the perturbation to the plasma frequency $\omega_{LC} = \sqrt{8E_C E_L}/\hbar$ of our LC-resonator, but instead to the plasma frequency of our CPB, $\omega_{JC} = \sqrt{8E_C E_J}/\hbar$, as we can neglect the influence of the inductive shunt in this limit and can instead consider the Josephson junction as an inductive component in the circuit. However, as discussed in the introduction, the inductive shunt is what enables us to screen the CPB in the first place even if our calculations show excellent screening in the regime $E_L \ll E_C$ for large Josephson energies, independent of E_L. This would suggest that an inductive shunt is not needed to screen the CPB, but without the inductive shunt, only whole Cooper pairs can cross from the superconducting island to the ground superconductor which makes screening impossible. Therefore, the limit $E_L \to 0$ should be the subject of further studies.

Appendix A

Brillouin-Wigner perturbation theory

This chapter will give a short overview of the Brillouin-Wigner perturbation theory in order to calculate the off-diagonal element Δ of a two-level system's Hamiltonian

$$\hat{H}_{n,n'} = \begin{pmatrix} E_n & \Delta \\ \Delta & E_{n'} \end{pmatrix}. \tag{A.1}$$

Using this theory is especially useful as it avoids a separate treatment of non-degenerate and degenerate levels [5]. Suppose we have an Hamiltonian $\hat{H}$ with energies E that can be divided into the unperturbed Hamiltonian $\hat{H}^0$ with eigenvalues ε and a small perturbation $\hat{V}$. We start by defining the projection operators for our specific problem as

$$\hat{P} = |n\rangle\langle n| + \left|n'\right\rangle\left\langle n'\right| \quad \text{and} \quad \hat{Q} = 1 - \hat{P} \tag{A.2}$$

and can therefore rewrite our entire Hamiltonian as

$$\hat{H} = \begin{pmatrix} \hat{H}_{PP} & \hat{H}_{PQ} \\ \hat{H}_{QP} & \hat{H}_{QQ} \end{pmatrix} \quad \text{with the eigenvectors} \quad \mathbf{\Psi} = \begin{pmatrix} |\Psi_P\rangle \\ |\Psi_Q\rangle \end{pmatrix} \tag{A.3}$$

using the definitions $\hat{H}_{PQ} = \hat{P}\hat{H}\hat{Q}$, $|\Psi_P\rangle = \hat{P}|\Psi\rangle$, and so on. The eigenvalue problem can now be written in the form

$$\hat{H}_{PP}|\Psi_P\rangle + \hat{H}_{PQ}|\Psi_Q\rangle = E|\Psi_P\rangle, \tag{A.4}$$

$$\hat{H}_{QP}|\Psi_P\rangle + \hat{H}_{QQ}|\Psi_Q\rangle = E|\Psi_Q\rangle. \tag{A.5}$$

If we solve Eq. (A.5) for $|\Psi_Q\rangle$ and insert our result in Eq. (A.4), we get

$$\left(\hat{H}_{PP} + \hat{H}_{PQ}\frac{1}{E - \hat{H}_{QQ}}\hat{H}_{QP}\right)|\Psi_P\rangle = E\,|\Psi_P\rangle\,. \tag{A.6}$$

With the relation $\hat{H} = \hat{H}^0 + \hat{V}$ and the help of the geometric series, we can rewrite this equation as

$$\underbrace{\left(\hat{H}^0_{PP} + \hat{V}_{PP} + \hat{H}_{PQ}\sum_{k=0}^{\infty}\left[\frac{1}{E - \hat{H}^0_{QQ}}\hat{V}_{QQ}\right]^k \frac{1}{E - \hat{H}^0_{QQ}}\hat{H}_{QP}\right)}_{\hat{H}_{n,n'}}|\Psi_P\rangle = E\,|\Psi_P\rangle\,. \tag{A.7}$$

The disadvantage of this equation is that the perturbed Energies E appear on both sides of it. Assuming that the diagonal elements of $\hat{H}_{n,n'}$ receive the same corrections, only the off-diagonal element will contribute to our band gap. To lowest non-vanishing order, we can then substitute $E \approx \varepsilon$ on the left side of our equation giving the result

$$\Delta = \frac{\langle n|\,\hat{V}\,|n-1\rangle\,\langle n-1|\,\hat{V}\,|n-2\rangle\cdots\langle n'+1|\,\hat{V}\,|n'\rangle}{(\varepsilon_n - \varepsilon_{n-1})(\varepsilon_n - \varepsilon_{n-2})\cdots(\varepsilon_n - \varepsilon_{n'+1})} \tag{A.8}$$

for our off-diagonal elements.

Appendix B

Calculations: wave packet

The following calculations of a wave packet apply for the harmonic regime in Sec. 4.1 where we can assume E_J to be zero and therefore use the Hamiltonian from Eq. (3.14) in our calculations. For our initial state at $t_0 = 0$, we will start with a normalized Gaussian wave packet around q_0 with width σ

$$\langle q|\Psi_0\rangle = \frac{1}{\sqrt{\sigma}\pi^{\frac{1}{4}}} \exp\left[-\frac{(q-q_0)^2}{2\sigma^2}\right]. \tag{B.1}$$

With the time evolution operator $\hat{U} = \exp(-it\hat{H}/\hbar)$, we can write

$$\langle q|\Psi\rangle = \langle q|\,\hat{U}\,|\Psi_0\rangle = \int_{-\infty}^{\infty} dq'\,\langle q|\,\hat{U}\,|q'\rangle\,\langle q'|\Psi_0\rangle \tag{B.2}$$

but in order to perform this integral we need the matrix elements $\langle q|\,\hat{U}\,|q'\rangle$ which can be calculated to [3]

$$\langle q|\,\hat{U}\,|q'\rangle = \sqrt{\frac{\tau}{2\pi i \sin(\omega t)}} \exp\left\{\frac{i\tau\left[(q^2+q'^2)\cos(\omega t) - 2qq'\right]}{2\sin(\omega t)}\right\} \tag{B.3}$$

using the substitutions $\tau = \sqrt{8E_C/E_L}$ and $\omega = \sqrt{8E_C E_L}/\hbar$ that we introduced in Ch. 3. Now, we can perform the integral by writing

$$\begin{aligned}\langle q|\Psi\rangle &= \underbrace{\sqrt{\frac{\tau}{2i\sigma\pi^{3/2}\sin(\omega t)}}}_{:=\,d} \int_{-\infty}^{\infty} dq' \exp\left(-\frac{q'^2}{a} + q'b + c\right) \\ &= \sqrt{\pi}\, d\, \sqrt{a} \exp\left(\frac{1}{4}\, b^2 a + c\right)\end{aligned} \tag{B.4}$$

where we used the following substitutions:

$$\begin{aligned} a &= \frac{2\sigma^2 \sin(\omega t)}{\sin(\omega t) - i\tau\sigma^2 \cos(\omega t)}, \\ b &= \frac{-2iq\tau}{2\sin(\omega t)} + \frac{q_0}{\sigma^2}, \\ \text{and} \qquad c &= \frac{i\tau q^2 \cos(\omega t)}{2\sin(\omega t)} - \frac{q_0^2}{2\sigma^2}. \end{aligned} \tag{B.5}$$

The probability density $|\Psi(q)|^2$ can now be simplified to

$$\begin{aligned} &|\Psi(q)|^2 = \sqrt{\frac{1}{\pi k_{\mathrm{qm}}}} \exp\left(-\frac{k_{\mathrm{cl}}}{k_{\mathrm{qm}}}\right) \\ &\text{with} \quad k_{\mathrm{cl}} = [q - q_0 \cos(\omega t)]^2 \\ &\text{and} \quad k_{\mathrm{qm}} = \frac{1}{\tau^2\sigma^2}\left[\sin^2(\omega t) + \tau^2\sigma^4 \cos^2(\omega t)\right], \end{aligned} \tag{B.6}$$

which is the result from Eq. (4.1) in Sec. 4.1.

Another way to analyze this problem is to make the re-substitution $q \to n + p$ in our probability density, see Sec. 3.3, and to add up all n. This way, we are calculating the diagonal elements of the reduced density matrix

$$\varrho(p, p') = \sum_{n=-\infty}^{\infty} \langle n + p|\Psi\rangle \left\langle \Psi \middle| n + p' \right\rangle. \tag{B.7}$$

For our specific problem, we can write

$$\begin{aligned} \varrho(p, p) &= \sum_{n=-\infty}^{\infty} |\Psi(n + p)|^2 \\ &= \sqrt{\frac{1}{\pi k_{qm}}} \exp\left[-\frac{(p - q_0 \cos(\omega t))^2}{k_{qm}}\right] \\ &\qquad \cdot \vartheta\left[\frac{i(p - q_0 \cos(\omega t))}{k_{qm}\pi}; \frac{i}{k_{qm}\pi}\right] \end{aligned} \tag{B.8}$$

whereas ϑ denotes the Jacobi theta function. Using the identity [10]

$$\vartheta(z; -1/x) = \vartheta(zx; x)\sqrt{\frac{x}{i}}\, e^{i\pi x z^2}, \tag{B.9}$$

we can rewrite our result as

$$\varrho(p, p) = \vartheta[-p + q_0 \cos(\omega t); ik_{qm}\pi]. \tag{B.10}$$

Acknowledgements

I want to thank my supervisor Prof. Dr. Fabian Hassler for introducing me to this interesting subject and making my work possible. I am thankful for the time he took to answer my questions and supporting me in the important steps of my work. In addition, I also want to thank Jascha Ulrich for helping me with all of my questions and proofreading this thesis.

Bibliography

[1] A. Barone and G. Paternò. *Physics and applications of the Josephson effect*. UMI Out-of-Print Books on Demand. Wiley, 1982.

[2] A. Down. *Debye Length*. http://people.duke.edu/∼ad159/files/p142/2.pdf, 2015/07/03.

[3] R. P. Feynman and A. R. Hibbs. *Quantum Mechanics and Path Integrals*. Dover Publications Inc., 1965.

[4] R. P. Feynman, R. B. Leighton, and M. L. Sands. *The Feynman Lectures on Physics, Desktop Edition Volume III: The New Millennium Edition*. Number Bd. 3. Basic Books, 2013.

[5] K. Ingersent. *Brillouin-Wigner Perturbation Theory*. http://www.phys.ufl.edu/∼kevin/teaching/6646/04spring/bw.pdf, 2015/07/11.

[6] J. Koch, V. Manucharyan, M. H. Devoret, and L. I. Glazman. *Charging effects in the inductively shunted Josephson junction*, volume 103. Phys. Rev. Lett. **103**, 7004, 2009.

[7] L. D. Landau and E. M. Lifshitz. *Quantum Mechanics Non-Relativistic Theory, Third Edition: Volume 3 (Course of Theoretical Physics)*, volume 47. 1977.

[8] J. Rauch. *Fourier Series, Integrals, and, Sampling From Basic Complex Analysis*. http://www.math.lsa.umich.edu/∼rauch/555/ fouriercomplex.pdf, 2015/07/11.

[9] J. R. Rubbmark, M. M. Kash, M. G. Littman, and D. Kleppner. *Dynamical effects at avoided level crossings: A study of the Landau-Zener effect using Rydberg atoms*. Number 6. Phys. Rev. A **23**,3107, 1981.

[10] E. M. Stein and R. Shakarchi. *Complex Analysis*. Princeton lectures in analysis. Princeton University Press, 2010.

[11] D. van Delft and P. Kes. *The discovery of superconductivity.* https://www.lorentz.leidenuniv.nl/history/cold/DelftKes_HKO_PT.pdf, 2015/06/26.